

VERTICAL STRUCTURE IN PLUTO'S ATMOSPHERE FROM THE 2006 JUNE 12 STELLAR OCCULTATION

E. F. YOUNG¹, R. G. FRENCH^{2,11}, L. A. YOUNG¹, C. R. RUHLAND¹, M. W. BUIE³, C. B. OLKIN¹, J. REGISTER⁴, K. SHOEMAKER^{5,11},
G. BLOW⁶, J. BROUGHTON⁷, G. CHRISTIE⁸, D. GAULT⁹, B. LADE¹⁰, AND T. NATUSCH⁸

¹ Department of Space Studies, Southwest Research Institute, 1050 Walnut St, Suite 300, Boulder, CO 80302, USA

² Department of Astronomy, Wellesley College, Wellesley, MA 02481, USA

³ Lowell Observatory, 1400 W. Mars Hill Rd., Flagstaff, AZ 86001, USA

⁴ Greensboro Day School, 5401 Lawndale Drive, Greensboro, NC 27455, USA

⁵ Shoemaker Labs, Lafayette, CO 80026, USA

⁶ Occultation Section, Royal Astronomical Society of New Zealand, PO Box 3181, Wellington, New Zealand

⁷ Reedy Creek Observatory, Reedy Creek, Queensland, Australia

⁸ Auckland Observatory, PO Box 24 180 Royal Oak, Auckland 1345, New Zealand

⁹ Hawkesbury Heights, New South Wales, Australia

¹⁰ Stockport Observatory, South Australia, Australia

Received 2007 December 27; accepted 2008 June 20; published 2008 September 26

ABSTRACT

Pluto occultations are historically rare events, having been observed in 1988, 2002, 2006, and, as Pluto moves into the crowded Galactic plane, on several occasions in 2007. Here we present six results from our observations of the 2006 June 12 event from several sites in Australia and New Zealand. First, we show that Pluto's 2006 bulk atmospheric column abundance, as in 2002, is over twice the value measured in 1988, implying that nitrogen frost on Pluto's surface is 1.2–1.7 K warmer in 2006 than 1988 despite a 9% drop in incident solar flux. We measure a half-light shadow radius of 1216 ± 8.6 km in 2006, nominally larger than published values of 1213 ± 16 km measured in 2002. Given the current error bars, this latest half-light radius cannot discriminate between continued atmospheric growth or shrinkage, but it rules out several of the volatile transport scenarios modeled by Hansen & Paige. Second, we resolve spikes in the occultation light curve that are similar to those seen in 2002 and model the vertical temperature fluctuations that cause them. Third, we show that Pluto's upper atmosphere appears to hold a steady temperature of ~ 100 K, as predicted from the methane thermostat model, even at latitudes where the methane thermostat is inoperative. This implies that energy transport rates are faster than radiational cooling rates. Fourth, this occultation has provided the first significant detection of a non-isothermal temperature gradient in Pluto's upper atmosphere also reported by Elliot et al., possibly the result of CO gas in Pluto's upper atmosphere. Fifth, we show that a haze-only explanation for Pluto's light curve is extremely unlikely; a thermal inversion is necessary to explain the observed light curve. And sixth, we derive an upper limit for the haze optical depth of 0.0023 in the zenith direction at average CCD wavelengths.

Key words: occultations – planets and satellites: individual (Pluto)

Online-only material: color figure

1. INTRODUCTION

1.1. Previous Occultations

Our collective understanding of Pluto's atmosphere is largely based on occultation observations. Pluto's atmosphere was first detected from a 1985 stellar occultation (Brosch & Mendelson 1985) and a detailed profile derived from a 1988 occultation that was observed from the Kuiper Airborne Observatory (KAO, see Figure 1) and other sites (Elliot & Young 1992). Even a thin atmosphere like Pluto's will produce a gradual decrease in the brightness of the occulted star due to refraction and absorption. In the 1988 KAO light curve, the initial roll-off is consistent with differential refraction in Pluto's clear upper atmosphere, but the light curve's inflection point at a radius of 1215 km has been variously interpreted as a thermal inversion or a low-altitude haze layer.

Pluto's perihelion occurred in 1989 September, shortly after the 1988 occultation, when Pluto's subsolar latitude was just south of its equator (using the IAU definition of north). Two more events observed in 2002 showed that Pluto's bulk atmosphere

had doubled since 1988, despite the fact that Pluto has been receding from the Sun since 1989 (Sicardy et al. 2003; Elliot et al. 2003). Seasonal change/volatile transport models by Hansen & Paige (1996) are consistent with increased frost temperatures in the post-perihelion decade, but the general expectation is that Pluto's atmosphere will enter a bulk condensation phase in the near future. From the 2006 occultation, it appears that Pluto's column abundance has not changed significantly since 2002.

1.2. Occultations as Atmospheric Probes

Stellar occultations are sensitive probes of Pluto's atmospheric temperature, density, and pressure profiles. As Pluto's atmosphere moves in front of an occulted star, the light from the star is refracted by Pluto's atmosphere. The angular deviation of the star's rays is greatest for rays which traverse chords through the lower portions of the atmosphere, where the density gradient is exponentially greater. This phenomenon, the spreading out of the star's rays as a function of the altitude at which they impact Pluto's atmosphere, is called differential refraction. Because of differential refraction, Pluto's atmosphere (and exponential atmospheres in general) act as weak divergent lenses.

¹¹ Visiting Astronomer, Anglo-Australian Telescope.

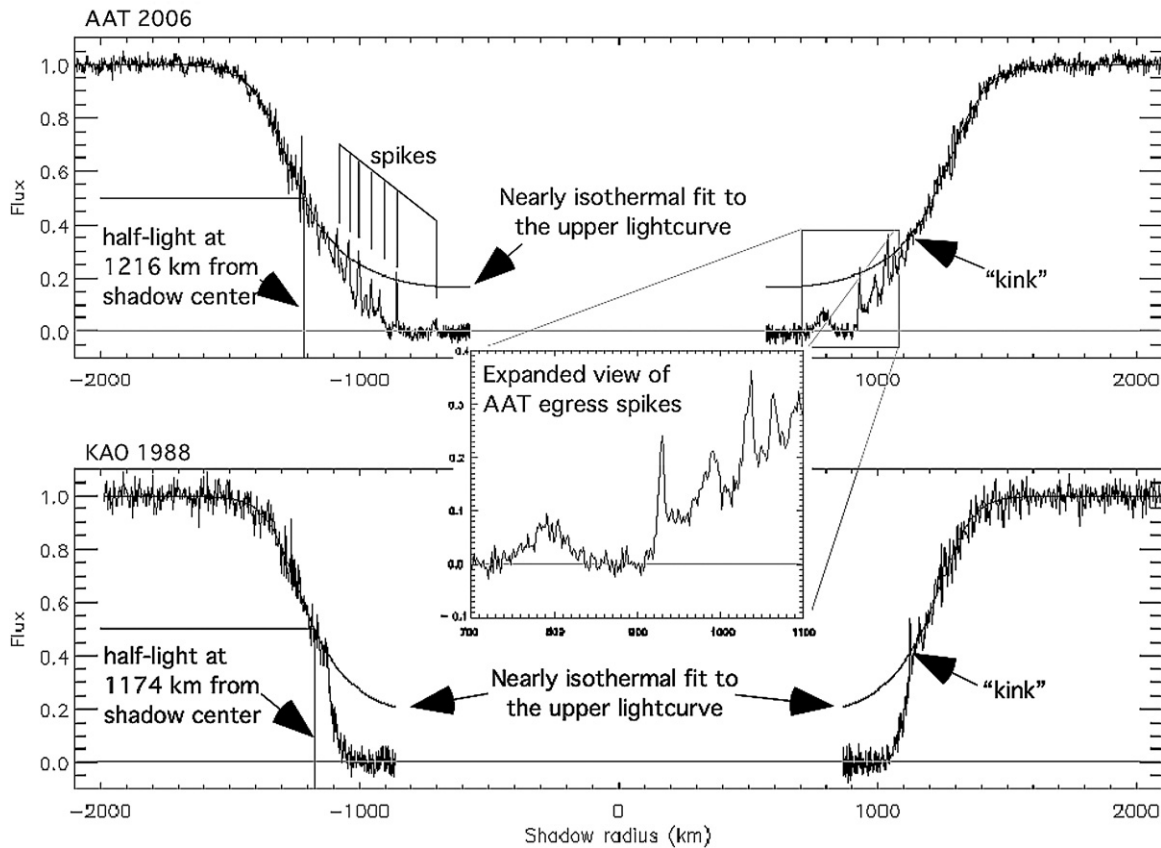


Figure 1. A comparison of two stellar occultations by Pluto. A 2006 light curve (top) and a 1988 light curve show several distinctive changes. First, the half-light radius increased between 1988 and 2002, and continues at the 2002 level in 2006. Second, the 2006 light curve also departs from the isothermal model that fits the upper atmosphere well, but the kink in 2006 is much less abrupt than in 1988. Third, there are resolved spikes observed during ingress and egress in the 2006 light curve, including two broad humps seen between 800 and 900 km in the shadow radius. The KAO data set does not show these spikes in the lower parts of the 1988 light curve.

Some atmospheres contain fluctuations in their mainly exponential density profiles. In these cases, local density perturbations can produce convergent focusing of some of the star's rays. As focused rays pass over ground-based telescopes, they produce bright spikes in the occultation light curve. In our Anglo-Australian Telescope (AAT) light curve, we see multiple spikes that are resolved by at least five to ten data points; these are the most compelling evidence to date on the size and extent of temperature fluctuations in Pluto's atmosphere. Sicardy et al. (2003) and Pasachoff et al. (2005) reported spikes in their light curves as well, although at lower signal-to-noise ratio (S/N) and time resolution than in the AAT light curve.

It is possible to construct a simple atmospheric model based on a few free parameters, such as a temperature gradient or a haze optical depth over certain ranges of altitudes. Clear, nearly-isothermal models have closely fit the upper atmosphere of Pluto with temperatures near 100 K for both ingress and egress, in all occultation light curves (in 1988, 2002, and 2006) of which we are aware. However, the models which fit Pluto's upper atmosphere are inconsistent with Pluto's lower atmosphere. The cause of the discrepancy has been variously attributed to haze, a thermal inversion, or a combination of the two (e.g., Elliot & Young 1992; Eshelman 1989). We will show that a haze-only solution is not tenable.

There are two complementary techniques which we use to transform light curves into density, pressure, and temperature profiles. The first is mentioned in the previous paragraph: a forward model, typically based on a few free parameters

(six, in our case). The second is called the inversion method, a bootstrap determination of refractivities from high to low altitudes, beginning with an upper boundary condition and progressing downward on a point-by-point basis in lockstep with the observed fluxes. Without a boundary condition (e.g., an upper boundary provided by the forward model's fit to the upper atmosphere), the inversion method could not determine density (or temperature) versus altitude, only density or temperature gradients versus altitude.

1.3. New Results

The observations and data reduction pipeline are discussed in Section 2, primarily describing how the collected images are turned into one-dimensional light curves with propagated errors and how the light curves determine the geometric solution. The analysis and results section (Section 3) describes how light curves map to temperature, density, and pressure profiles, and what those profiles are.

We then discuss five significant results from the 2006 June 12 occultation in Section 4 as follows. First, we derive a half-light radius (a measure of Pluto's column abundance) which, in the context of previous occultation half-light radii, indicates whether Pluto's atmosphere is expanding or shrinking. Second, we derive temperature profiles from regions of Pluto's atmosphere sampled at the star's ingress and egress. These first two results are similar to work presented by other investigators following the occultations in 2002 and 2006 (e.g., Elliot et al. 2003; Sicardy et al. 2003; Elliot et al. 2007 with respect to

Table 1
Observing Circumstances for the Five Sites that Contributed to this Paper

Site	Location	Impact Parameter ^a (km)	Exp. Time/ Duty Cycle (s)	S/N ^b	Weather	Observers
REE ^c	28°06'36" S 153°23'49" E	836.6 (N)	15.0/22.5	5.4	Clear	JB
AAT ^d	31°16'37" S 149°03'58" E	571.8 (N)	0.1/0.1	333	Clear	RGF, KS
STO ^e	34°19'55" S 138°43'45" E	382.2 (N)	1.0/2.0	14	Clear	BL
HHT ^f	33°39'52" S 150°28'38" E	302.5 (N)	1.0/2.0	3.6	Clear	DG
CAR ^g	41°17'03" S 174°45'55" E	-857.6 (S)	0.65/0.56	7.7	Cumulus, icy cirrus	MWB, CRR

Notes.

^a The impact parameter is the minimum distance from a site to the shadow's center.

^b S/N is the signal-to-noise ratio in the unocculted signal over an interval during which Pluto's shadow moves 60 km, or approximately one scale height.

^c REE = Reedy Creek Observatory, QLD, AUS (0.5 m aperture).

^d AAT = Anglo-Australian Observatory, NSW, AUS (4 m).

^e STO = Stockport Observatory, SA, AUS (0.5 m).

^f HHT = Hawkesbury Heights, NSW, AUS (0.2 m).

^g CAR = Carter Observatory, Wellington, NZ (0.6 m). Observations were also attempted at Auckland Observatory (GC, TN); Campbell Farm in Longford, Tasmania (EFY, JR); and Gillespie Farm, Wanaka, NZ (CBO, LAY).

Pluto's half-light radii, and Sicardy et al. 2003 with respect to Pluto's temperature profile).

Third, we present a new constraint on radiative heating and cooling rates relative to dynamical timescales in Pluto's upper atmosphere, and fourth, we determine a non-isothermal temperature gradient in Pluto's upper atmosphere. Finally, we provide new evidence against a haze-only solution to explain the attenuation seen in the lower-atmosphere part of Pluto's occultation light curve, and present an upper limit to the one-way haze optical depth from the haze-only solution.

2. OBSERVATIONS

Several research teams deployed observers to southern latitudes to observe Pluto move in front of a 15.5 mag star (P_{384.2} from McDonald & Elliot 2000a, 2000b) on 2006 June 12. Our team of PHOT observers successfully observed this event from various sites, including the 3.9 m AAT in Siding Spring under clear skies (Table 1). The AAT observations produced a light curve with an unprecedentedly high S/N.

Observations were also attempted at Auckland Observatory (GC, TN), Campbell Farm in Longford, Tasmania (EFY, JR), and Gillespie Farm, Wanaka, NZ (CBO, LAY).

2.1. Photometric Reduction

2.1.1. Reduction of the Anglo-Australian Telescope Data Set

The AAT observations were taken unfiltered with one of our PHOT (portable high-speed occultation telescope) cameras, a Princeton Instruments MicroMax BFT512 frame-transfer CCD with low read noise (approximately 3.1 e- per read) and virtually no dead time (~2 ms) between exposures at the 10 Hz frame rate used for this event. Conditions were clear with excellent seeing. Despite the fact that Pluto was only 10° away from the full moon, the background was remarkably free of scattered light, perhaps because a storm on the previous day may have removed suspended particulates. The small field of view of 44" included Pluto and the occultation star plus two comparison

stars. (In this section, in the context of photometric reduction, we use "Pluto" as a shorthand for the entire Pluto system, i.e., Pluto, Charon, Nix, and Hydra). The platescale at the AAT's *f*/8 auxiliary instrument ports is 0.087" pixel⁻¹ at full resolution, or 0.348" pixel⁻¹ with the 4 × 4 binning that was used for the event. The reduction pipeline consisted of the following steps.

1. Each frame was dark-subtracted using 0.1 s dark frames, the same exposure time as the occultation observations, and normalized by the flat-field.
2. Photometry of Pluto and two on-chip comparison stars within the 44" field of view was performed with the IDL routine *BASPHOTE.PRO*, part of Marc Buie's library of IDL routines 2007¹². This routine performs circular aperture photometry with user-specified apertures for the object and the sky annulus. A range of aperture radii were tested for the object's aperture and the inner and outer sky radii. An aperture radius of 4 pixels (1.4") and inner and outer sky radii of 10 and 14 pixels were chosen as the aperture sizes that minimized rms noise in the pre- and post-event segments of the occultation light curve. *BASPHOTE* estimates the noise for each pixel and propagates that error to the fluxes determined for each object.
3. Individual photometry of Pluto and the occultation star (P_{384.2}) was obtained from images acquired prior to 1.5 h before the event, when the separation between the two objects was 5" or greater. The ratio of Pluto to Pluto-plus-P_{384.2} was 0.682 ± 0.003.
4. The flux from Pluto-plus-P_{384.2} was normalized by the sum of fluxes from the comparison stars. Although sky conditions were good, the comparison stars' fluxes exhibited slowly changing variability on the few-percent level. The comparison stars' light curves were each smoothed by convolving them with a triangular kernel with a FWHM of

¹² <http://www.boulder.swri.edu/~buie/idl/>

- 1.0 s. Kernel widths of 0.5–1.5 s were tested, with 1.0 s chosen as the kernel that minimized the rms noise in the pre- and post-event segments of the occultation light curve.
5. The occultation light curve (Pluto-plus- $P_{384.2}$ divided by the sum of comparison star fluxes) and associated errors were normalized such that the flux level without $P_{384.2}$ is 0.682 times the out-of-event baseline flux.

2.1.2. Reduction of the Carter Observatory Data Set

Like the AAT observations, the Carter Observatory data set was taken with a PHOT camera, but at a 1 Hz frame rate instead of a 10 Hz rate. In addition, the conditions in Wellington were variably cloudy and the background (clouds illuminated by moonlight) was much more significant than for the AAT exposures. As a result, the data reduction pipeline has several steps not found in the AAT pipeline. The Carter Observatory pipeline was as follows.

1. Each frame had a bias frame and a model of the background subtracted from it. The background was modeled as a second-order, six-term polynomial in CCD x and y coordinates.
2. For clear frames, the centers of Pluto, $P_{384.2}$, and comparison stars were determined by fits to the peaks of each object in individual frames. For cloudy frames, as many as ten frames were co-added, then the centers of the brightest stars were found in the co-added frame and the centers of Pluto and other comparison stars were located using known offsets from the brightest stars in the field.
3. The flux from each source was determined by point-spread function (PSF) fitting. The PSF was assumed to be a circular gaussian. The full width at half-maximum (FWHM) of the gaussian was a single fitted parameter for the entire frame. Each individual source had three additional fitted parameters: the x and y centers and the total flux from that source. Errors were propagated in much the same way as in the AAT pipeline: per-pixel errors were estimated as the quadratic sum of “sky noise” and Poisson source noise, then propagated for the PSF that was used to model each individual source.
4. An inverse linear relation was found between the background counts around an object and the flux from the object itself, basically describing how the background counts increased and the star counts decreased in the presence of clouds. This relationship was used to correct for variable cloudiness during the event (i.e., background counts were used in the cloudiest frames to estimate the counts from Pluto, $P_{384.2}$ and the comparison stars).
5. As in the AAT pipeline, the ratio of Pluto to Pluto-plus- $P_{384.2}$ was determined from pre-event observations (which were cloud-free) 90 minutes before the event or earlier. The ratio $\frac{P}{(P+P_{384.2})}$ was determined to be 0.685 ± 0.003 . The Carter light curve (Pluto-plus- $P_{384.2}$ divided by the sum of the comparison stars) was normalized such that the flux ratio of Pluto-plus- $P_{384.2}$ to Pluto was 1:0.685.

2.1.3. Reduction of the Hawkesbury Heights Data Set

Photometry from the 1 Hz Hawkesbury Heights image series, as with the AAT images, was extracted using aperture photometry (BASPOTE.PRO).

1. After examining a range of aperture sizes, an object aperture of 4 pixels was used, along with a sky annulus with inner and outer radii of 10 and 15 pixels, respectively.
2. The three brightest comparison stars’ light curves were smoothed by convolving them with a triangular kernel with a FWHM of 1.5 s.
3. The depth of the event (Pluto divided by Pluto-plus- $P_{384.2}$) was determined to be 0.693 for this observatory.

2.1.4. Reduction of the Reedy Creek and Stockport Data Sets

The images at Reedy Creek and Stockport were both obtained with Meade Deep Sky Imager (DSI) II CCDs. These detectors save interleaved frames consisting of even and odd rows that partially overlap in time. Both sites acquired 1 s exposures every two seconds. The observations were time-stamped with a KIWI-OSD GPS-based video time inserter.

The interleaved odd and even frames overlap in time. We had tried to extract photometric brightnesses from individual odd and even frames in an attempt to double the time resolution, but we decided that the S/N degradation that resulted from separate odd and even light curve extraction was not worth the increase in time resolution. As with the image sequences from the other sites, we used aperture photometry on combined odd/even pairs, and assigned image mid-times that were averages of the odd-frame and even-frame mid-times.

The light curves from the 0.5 Hz Reedy Creek and Stockport image series were processed as follows.

1. The sub-pixel estimates of Pluto centers were refined using BASPHOTE.PRO in each frame.
2. BASPHOTE.PRO was used to extract aperture photometry of Pluto, with an object aperture radius of 4 pixels and a background annulus ranging from 10 to 15 pixels in radius. A range of apertures were tested; these apertures produced the lowest rms variation in the pre- and post-event baseline segments of the light curve.
3. Six on-chip comparison stars were initially selected, but only the three brightest were eventually used for normalization. These are the same three comparison stars used for the Hawkesbury Heights reduction. The centers to the stars were estimated using known offsets to Pluto’s center, then refined with BASPHOTE.PRO.
4. Before the signal from the comparison stars were used for normalization, they were summed and then smoothed by convolving them with a triangular kernel with a FWHM of 20 s. The smoothed comparison star signals were then used to normalize the Pluto light curve.
5. The ratio of Pluto to Pluto-plus-star was provided to us separately by the observers (D. Gault, Reedy Creek; B. Lade, Stockport). The normalized light curves were scaled to 1 (upper baseline) and $\frac{P}{(P+P_{384.2})}$ (lower baseline).

2.2. The Geometric Solution: Determining Pluto’s Shadow Path

During a stellar occultation, Pluto casts a faint stellar shadow that moves across the Earth. We determine the precise path of this shadow as a necessary precursor to determining the vertical structure of Pluto’s atmosphere. In general, this task requires groundstations that are well-separated from the central chord of the shadow and each other. Our data set spans 82% of

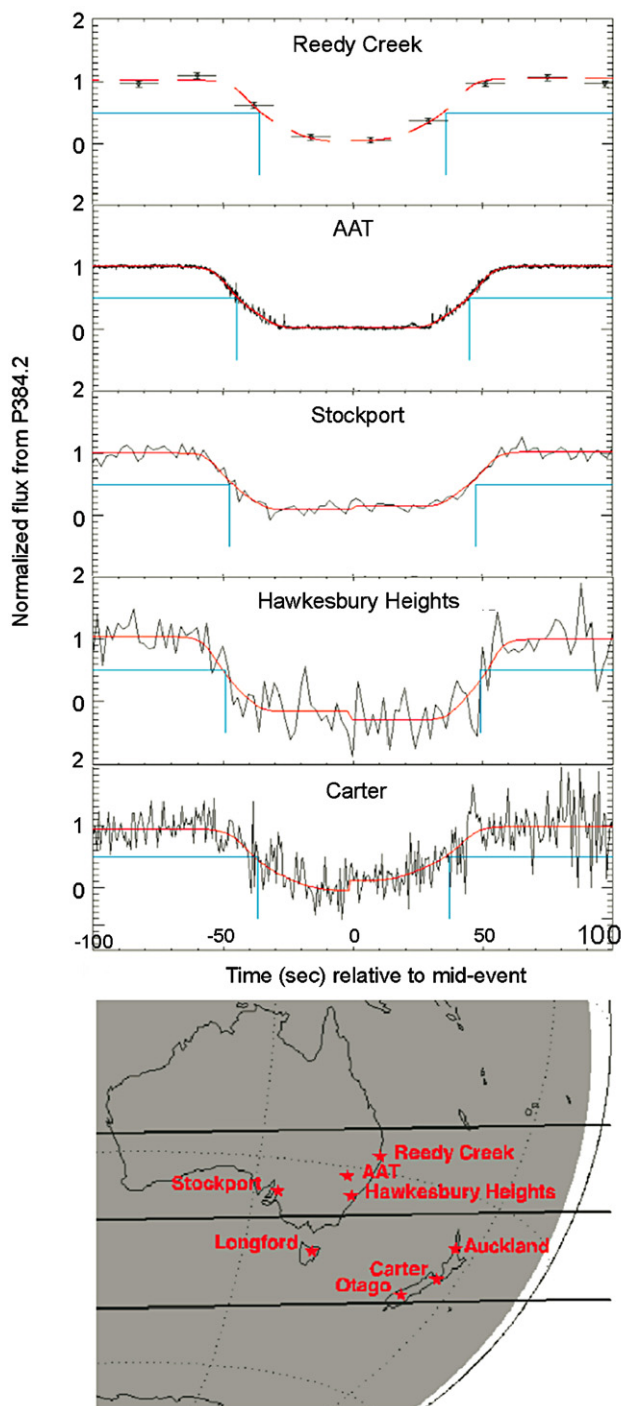


Figure 2. Light curves from the five sites used in this paper. For each of the five light curves the AAT-based templates are shown as red overlays; note that separate templates were used for ingress and egress. The half-light times are marked by blue lines.

Pluto's diameter (Figure 3). It consists of one low-noise light curve (AAT) and four noisier light curves obtained from smaller telescopes in Australia and New Zealand (Figure 2).

The precursor to finding the geometric solution is to find the half-light times of each light curve. Because the S/N of the AAT light curve is so much higher than that from our other sites, we decided to build a template from the AAT light curve and fit that template, adjusted in shape to account for the occultation geometry of each site, to the other four light curves. This template is actually a six-parameter model of a

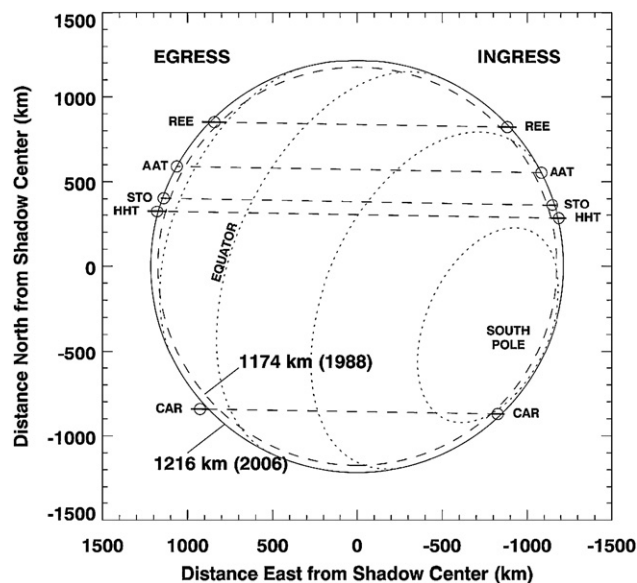


Figure 3. The geometric solution in graphical form. While the AAT light curve was the only one with a sufficiently high S/N to produce temperature and density profiles of Pluto's atmosphere, the light curves from small telescopes at distant locations were essential to reconstructing the path of Pluto's shadow over the Earth.

near-isothermal atmosphere (described in detail in Section 3.2), which we evaluate at the five observing sites to generate site-specific model light curves.

We determine the geometric solution from the half-light times (the times during ingress and egress when the observed flux is halfway between the full flux the occulted star and zero flux from the occulted star). The geometric solution describes where Pluto's shadow passed over the Earth. It is equivalent to finding f_0 and g_0 , the offsets to the nominal Pluto-star separation which were based on the reference position of the star and the reference ephemeris of Pluto. Alternatively, f_0 and g_0 are the measured shadow center offsets in right ascension and declination relative to the center that was predicted from the reference positions of the star and Pluto (i.e., they are the measured corrections to the predicted shadow center position).

We determine the half-light times with an iterative procedure. The six-parameter fit to the AAT light curve (following Elliot & Young 1992 and described in Section 3.1) depends on assumed values for f_0 and g_0 , yet we use the AAT-based template to fit for half-light times and improved values for f_0 and g_0 . We iterate to find f_0 and g_0 as follows.

1. We begin with a graphical exercise to get a ball-park estimate for g_0 . Specifically, we plot the chords from each site as they would appear on the Earth, but shifted so that their approximate mid-times are aligned. We overlay disks corresponding to Pluto's projected shadow while varying g_0 (i.e., while moving the shadow's path north or south) until we find a disk that appears to match the ingress and egress from each site. This exercise produced a rough initial guess for g_0 of -1024 km, not too far from our eventual value of $g_0 = -1111$ km.
2. We next perform a parameter search in g_0 space using 50 km increments. For each g_0 value, we fit a six-parameter atmospheric model to the AAT light curve.
3. After solving for a six-parameter atmospheric model, we generate model light curves for the other four sites. The model light curves are shifted in time to match the observed

Table 2
Half-Light Times

Site	Half-light Time ^a (ingress)	Half-light Time ^a (egress)
REE	1344.676 ± 2.22	1416.596 ± 3.00
AAT	1354.940 ± 0.05	1444.390 ± 0.05
STO	1391.968 ± 0.93	1487.278 ± 0.66
HHT	1348.360 ± 1.90	1447.050 ± 2.34
CAR	1314.080 ± 1.64	1387.570 ± 2.27

Note. ^a Half-light times in seconds after 16:00:00 UT.

upper and lower baselines from each site. The model light curves are intended to be smoothed fits to long sequences of noisy observations; we can derive more robust half-light times from the fitted model light curves than from the noisy observations.

4. We now have half-light times for the AAT and the four other sites for each of the g_0 grid-point values. If a g_0 value is too far north or south, then some (but not necessarily all) of the light curves will be too long or too short in duration. We choose the g_0 value that minimizes the discrepancies between the model and observed light curves.
5. With a new estimate for g_0 , we return to step 2 to fit a new six-parameter model to the AAT light curve and evaluate a grid of possible g_0 values using the new model light curves. We stop the procedure when the change in half-light times is less than a tenth of a second from the previous iteration.
6. After converging on a set of ten half-light times (Table 2), we generate our final values for Pluto's half-light radius and f_0 and g_0 .

In 1988 Pluto's half-light shadow radius was 1174 ± 20 km (Elliot & Young 1992). By 2002 Pluto's half-light radius had increased to 1213 ± 16 km (Sicardy et al. 2003; Elliot et al. 2003). We now determine a half-light shadow radius of 1216.0 ± 8.6 km from the 2006 June 12 event.

3. ANALYSIS AND RESULTS

3.1. Pluto's Atmosphere by Parametric Fitting

We use two standard techniques for retrieving temperature and pressure profiles from the AAT light curve: a forward model in which parameters that describe a model atmosphere are adjusted to minimize the sum of weighted, squared residuals between the observed light curve and one generated from the model atmosphere (Baum & Code 1953; Elliot & Young 1992) and the inversion method, a bootstrap determination of refractivities from high to low altitudes, beginning with an upper boundary condition and progressing downward on a point-by-point basis in lockstep with the observed fluxes (French et al. 1978; Elliot et al. 2003; Roques et al. 1994).

Which haze profile is required to fit the 2006 and 1988 light curves under the assumption that the nearly isothermal atmosphere extends down to the minimum altitude that we observe? In other words, which haze profile explains the light curves' departures from the nearly isothermal profile that was determined from the forward model using points above the 0.6 flux level? We use the same forward model as Elliot & Young (1992), which consists of the following equations and assumptions.

1. Gravity varies as $1/r^2$.
2. The atmosphere is in hydrostatic equilibrium.

3. The occultation flux includes the small planet term, consisting of refocused starlight perpendicular to the gravity gradient (as opposed to the typical large planet practice of modeling the atmosphere as a cylinder).
4. The molecular weight is constant with height.
5. The temperature profile has at most a small gradient, which we have cast into a functional form $T(r) = T_0(r/r_0)^b$.
6. A haze layer characterized by three fitted parameters: an altitude cap, a scale height (includes a $1/g$ dependence), and an extinction (κ_2) at a reference altitude.

The six parameters are the temperature T_0 , the pressure P_0 , and the thermal gradient dT_0/dr , all evaluated at a reference radius $r_0 = 1275$ km, plus three parameters to describe a haze distribution: a cap (or ceiling) to the haze r_1 , a haze scale height H_{haze} at a reference altitude of $r_2 = 1200$ km, and extinction for the haze κ_2 evaluated at r_2 . The model temperature profile has the form $T(r) = T_0(r/r_0)^b$, and $P(r)$ is in hydrostatic equilibrium. These parameters are presented in Table 3, along with parameters which we have re-fit to the 1988 occultation light curve obtained from the KAO.

The simplest representation of the temperature gradient would be a constant. However, an isothermal atmosphere is incompatible with the observations; the residuals between the light curve observations and the best-fit model (with five free parameters and b set to zero) are about three times larger than the light curve errors. We use the simplest functional form that we can to accommodate a constant, non-zero thermal gradient: $T(r) = T_0(r/r_0)^b$. The use of other functional forms with more degrees of freedom may yield different solutions for dT/dr , but our S/N does not justify more complicated models for $T(r)$.

The pressure at the reference altitude of $r_0 = 1275$ km is 2.26 ± 0.32 times higher in 2006 than in 1988. Since Pluto's atmosphere is supported by the vapor pressure of nitrogen frost, the surface temperature of N_2 frost must be 1.2–1.7 K warmer in 2006 than in 1988 (Brown & Ziegler 1980). In addition, the temperature gradient dT/dr at r_0 is -0.086 ± 0.033 K km⁻¹, compared to the dry adiabat at r_0 of -0.6 K km⁻¹ (Figure 4D). The thermal profile in the upper atmosphere is slightly negative, but the atmosphere is statically stable over the entire region that we have retrieved, approximately 1198–1350 km under the assumption of a clear atmosphere.

3.2. Pluto's Lower Atmosphere by Light Curve Inversion

We determine the structure of the lower atmosphere with the inversion method for the portion of the light curve below 1260 km in the shadow radius (1302 km in Pluto radius). The inversion method assumes a clear atmosphere, geometric optics, no ray crossing, and a point source for the star. The upper boundary conditions are determined with a three-parameter forward model (identical to the six-parameter model except that the clear atmosphere has no haze parameters) using points above 1260 km, corresponding to the 0.6 flux level as recommended by French et al. (1978). Given the clear atmosphere assumption, both ingress and egress show a major change in the temperature gradient between Pluto radii of 1205 to 1240 km. The spikes correspond to temperature fluctuations below 1230 km, most of which have vertical extents of about 5 km and magnitudes less than 0.5 K, except for the large spikes at the lowest altitudes (Figures 4 and 5).

The ingress and egress light curves from the AAT are qualitatively the same, although different in detail. The overall similarity is somewhat surprising, given that the ingress latitude was only 6° south of the subsolar latitude, while the egress point

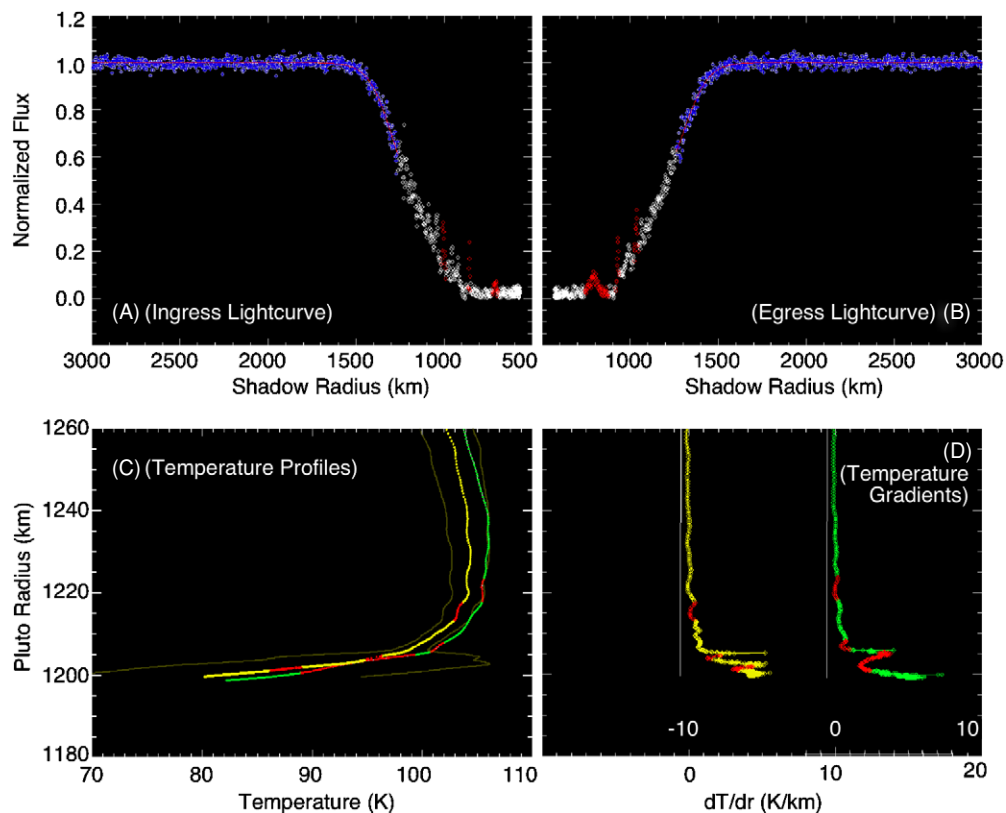


Figure 4. Ingress and egress light curves are shown in the top two panels. The blue points have been used to fit a three-parameter, nearly isothermal clear atmosphere model. This model provides upper boundary conditions for the light curve inversion. We have tagged some spikes in red to show that spikes in the light curves correspond to small thermal perturbations (or, equivalently, perturbations in the index of refraction). The lower left panel shows yellow and green $T(z)$ profiles (ingress and egress, respectively) with a large temperature inversion taking place around $z = 1210$ km, below which T decreases with descending altitude. The 1σ envelope is shown as faint yellow lines. The temperature gradients (lower right) show perturbations that are typical of gravity waves seen in occultations by Jupiter or Titan (e.g., Young et al. 2005).

Table 3
Best-fit Parameters for Pluto's Upper Atmosphere

Parameter	2006	2006	2006	1988	Units
	Ingress	Egress	Average	KAO	
T_0^a	100.0 ± 4.2	106.4 ± 4.6	103.9 ± 3.2	104.0 ± 7.3	(K)
P_0^a	1.76 ± 0.14	1.95 ± 0.15	1.86 ± 0.10	0.83 ± 0.11	(μ bar)
dT_0/dr^a	-0.113 ± 0.045	-0.082 ± 0.051	-0.086 ± 0.033	-0.040 ± 0.052	(K km $^{-1}$)
r_1	1286.8 ± 10.6	$1287.1 \pm 37.$	1273.6 ± 7.1	1215.8 ± 1.3	(km)
H_{haze}^b	16.6 ± 1.7	15.9 ± 1.8	15.9 ± 1.1	24.6 ± 4.2	(km)
κ_2^b	2.7 ± 0.5	3.0 ± 0.5	3.0 ± 0.4	4.1 ± 0.3	($1000 \times \text{km}^{-1}$)

Notes.

^a Value at a reference altitude of $r_0 = 1275$ km.

^b Value at a reference altitude of $r_2 = 1260$ km.

was less than 0.5° south of Pluto's arctic circle. The surprising similarities between the two light curves are discussed further in Section 4.4 in the context of the "methane thermostat."

As an aside, there are two reasons why Pluto's stellar occultations do not (and are not likely to) determine Pluto's solid radius. First, the mapping between the shadow radius and the inferred radius on Pluto is model dependent. In general, more haze in the atmospheric model will reduce the differences in the shadow radius-to-Pluto radius mapping, because haze can substitute for a steep refractive gradient as the cause of attenuation in the lower light curve, and refraction, not haze, causes the shadow radius to be smaller than Pluto's radius. Second, although we measure events in the shadow radius to altitudes that are certain to be at or below Pluto's solid surface,

we cannot use those data to determine Pluto's physical radius. The light from the occulted star is attenuated to nearly zero by differential refraction and haze long before Pluto's solid surface is a factor in the observed light curve. With extraordinarily high S/N, one could discern the differences between the lower baseline and zero flux from the star, but even with the AAT light curve's excellent S/N of 333 per 60 km, we can probe to only 1198 km (assuming a clear atmosphere). Part of the problem is our great distance from Pluto; differential refraction is a powerful attenuation mechanism when the spread of light takes place over 30 AU. An alternative would be to observe attenuation from much closer distances; the 1984–1990 mutual events (which effectively sampled Pluto's surface and atmosphere from Charon's distance of $\sim 20,000$ km) are a likely data set from

which Pluto's solid radius can be determined before the *New Horizons* flyby in 2015.

In other words, the limiting depth of an atmospheric retrieval depends on small flux differences in the lower baseline. In 1988, flux from the occultation star was detectable down to a shadow radius of 900 km (Elliot et al. 2003; Elliot & Young 1992), limited by the S/N and the determination of the lower baseline from pre- and post-event photometry of Pluto relative to the star. In 2006 we detected the star at shadow radii of 700 km and 778 km for immersion and emersion, respectively. For the clear-atmosphere case, the 1988 light curve probes down to 1204 km on Pluto, and the 2006 light curve probes down to 1198 km (immersion) and 1200 km (emersion).

The temperature gradient below 1205 km is large and positive, with dT/dr approximately equal to 2.5 K km^{-1} at the lower limit of the light curve (near 1200 km in Pluto radius). If this gradient continues, Pluto's atmosphere reaches 38–42 K, the spectroscopically measured temperature of Pluto's nitrogen frost in 1992 (Tryka et al. 1994; Grundy 1995), at a radius near 1180 km and a pressure near $13 \mu\text{bar}$. Since this pressure is less than the vapor pressure at Pluto's frost temperatures ($19 \mu\text{bar}$ at 38 K to $158 \mu\text{bar}$ at 42 K), Pluto may have a troposphere (a region in which the temperature gradient is close to the adiabat) of up to a few tens of km.

The source of the discontinuity in the 1988 light curve has been a contested question since its discovery—is it caused by a haze layer, a temperature inversion, or both? We address this question by examining the implications of the hypothetical haze distribution described in Table 2. The hypothetical 2006 haze distribution was determined in exactly the same way as the haze distribution presented in Elliot & Young (1992) for the 1988 light curve. We mathematically “remove” the haze by scaling the 2006 light curve at each timestep by $e^{\tau(s)}$, where $\tau(s)$ is the haze optical depth along the observer's instantaneous line of sight, s , to the star, and then apply the clear-atmosphere inversion method to the scaled light curve. Incidentally, this hypothetical haze distribution would not affect views of the surface by a spacecraft flyby. The haze optical depth would be a miniscule 0.0023 in the zenith direction (integrated from an assumed surface of 1160 km to the fitted haze cap at 1273.6 km).

We discuss the results of the haze layer experiment in more detail in Section 4.5. Briefly, the resulting temperature profile (after the haze is “removed”) has no thermal inversion—the temperature stays near 100 K down to the lowest probed radius, which is now 1160 km instead of 1198 km. We think a haze distribution that is extrapolated to the surface from the upper light curve parametric fit is untenable because extremely large temperature gradients would be required to connect the atmospheric temperature of 100 K at 1160 km to the nearby surface temperature of 38–42 K. There may be smaller amounts of haze present, but there must also be a temperature inversion. Future occultations need to be observed in both visible and infrared wavelengths to provide stronger constraints on haze properties.

3.3. A Qualitative Comparison: The 2006 June 12, CFHT (2002), and KAO (1988) Light Curves

In this section we compare our results to other observations of the 2006 June 12 occultation (Elliot et al. 2007). We also look at the time-evolution of Pluto's atmosphere with comparisons to the 2002 and 1988 occultations.

3.3.1. Comparison to other 12 June 2006 Observations

Elliot et al. (2007) observed the 2006 June 12 occultation from several sites in Australia and New Zealand. Their results are based on light curves obtained from Siding Spring, Black Springs, Stockport, Mt. Stromlo, and Hobart. Their highest S/N (96 per 60 km) is from the 5 Hz observations from the 2.3 m telescope at Siding Spring. Both our paper and Elliot et al. (2007) use the Stockport observations provided by B. Lade, but both groups performed separate photometric reductions of those data.

With respect to Pluto's upper atmosphere, there are some differences between our results and those of Elliot et al. (2007). Their preferred half-light radius (their fit 2) is $1208 \pm 4 \text{ km}$ in the shadow radius (1276.1 ± 3.5 in Pluto radius), compared to our half-light shadow radius of $1216 \pm 8.6 \text{ km}$. Our ingress and egress average temperature at 1275 km is $103.9 \pm 3.2 \text{ K}$, compared to $97 \pm 5 \text{ K}$ for Elliot et al. (2007) at their half-light radius of 1276.1 km. Their temperature gradient at 1276.1 km is $-0.17 \pm 0.05 \text{ K km}^{-1}$, compared to our value of $-0.086 \pm 0.033 \text{ K km}^{-1}$ at 1275 km; both are negative and significantly non-isothermal.

There is a qualitative difference between the 1988 to 2006 trend in our derived upper atmosphere temperatures (T_0) and the trend reported by (Elliot et al. 2007). We find that T_0 has been close to 104 K in every occultation observed from 1988 through 2006 (with typical errors of $\pm 3.0 \text{ K}$), but Elliot et al. (2007) report a significant cooling trend. They derive T_0 values at a reference radius of 1276 km of $114 \pm 10 \text{ K}$, $108 \pm 9 \text{ K}$, and $97 \pm 5 \text{ K}$ in 1988, 2002, and 2006, respectively.

We are at a loss to explain these differences, since both groups use nearly identical equations and free parameters in the forward model used to fit the upper atmosphere. It is unlikely that our separate geometric solutions could explain the discrepancy, since the sensitivity of T_0 to ρ_{\min} is

$$\frac{dT_{\text{iso}}}{d\rho_{\min}} = -T_{\text{iso}} \frac{\rho_{\min}}{\rho_h^2} \quad (1)$$

where ρ_h is the half-light shadow radius, ρ_{\min} is the shadow impact parameter, and T_{iso} is the temperature determined for an isothermal model of the upper atmosphere. This expression assumes that the error in ρ_h is much smaller than the error in ρ_{\min} .

For values of T_{iso} around 100 K, ρ_{\min} around 571 km (i.e., Siding Spring) and ρ_h around 1173 km, the sensitivity of T_{iso} to errors in ρ_{\min} is -0.043 K per km . In other words, a 10 km error in the shadow's central chord location translates to an upper atmosphere error of just -0.43 K . It is unlikely that our respective geometric solutions differ by more than 10 km, yet our nominal solutions for T_0 differ by about 10 K for the 1988 event and about 7 K for the 2006 event. Note that both we and Elliot et al. (2007) have independently re-analyzed the 1988 light curves for these post-2006 occultation papers.

Nor are the discrepancies in T_0 solutions likely to lie in different photometric calibrations. We derive a ratio of Pluto to Pluto-plus-P_{384.2} of 0.682 in our AAT observations (at Siding Spring), compared to 0.6727 for the 2.3 m Siding Spring light curve obtained by Elliot et al. (2007). This difference cannot explain the 7 K difference in our respective 2006 T_0 values. Finally, we note that our assumed value for the refractivity of N₂ is higher than that used by Elliot et al. (2007). Using the catalog magnitudes of the star, including the USNO B1.0 and GSC2.3.2, the quantum efficiency of our

cameras, and the known refractivity of N_2 (Cox 2000), we use a refractivity at STP of $2.96e-4$, similar to the refractivity of $2.98e-4$ used for the analysis of the 1988 Pluto occultation (Elliot et al. 2003; Elliot & Young 1992). This differs from Elliot et al. (2007), who use a value of $2.82e-4$. These differences remain to be reconciled.

3.3.2. Comparison to 2002 and 1988 Occultations

There are three characteristics of the 2006 light curve worth noting in comparison to earlier light curves.

1. Like the 2002 light curves, the 2006 light curves imply a surface pressure that is over twice as high as measured in 1988.
2. Like the 2002 light curves, the 2006 light curves exhibit spikes that are typical of vertical temperature variations. These spikes are not seen in the 1988 observations below the “kink” in the light curve, although the KAO light curve did resolve three spikes in the upper atmosphere, above the kink (Elliot & et al. 1989).
3. The 2006 and 2002 light curves do not show a pronounced “kink” at 1215 km, although their lower altitudes do deviate from the near-isothermal model that fits the upper atmosphere well in all occultations observed to date.

If the spikes are a manifestation of gravity waves in Pluto's lower atmosphere, then it is curious that the spikes were not seen in 1988; the S/N of the 1988 light curve is sufficient to have shown the AAT-sized spikes if they were present. In other words, among the other changes that occurred since 1988 (doubling of the bulk atmosphere and change in the shape of the troposphere that produces the “kink”), apparently something occurred that may be producing gravity waves.

4. DISCUSSION

4.1. The Evolution of Pluto's Half-Light Radius

The primary result from this and all previous stellar occultations by Pluto is the half-light radius of Pluto, a measure of Pluto's column abundance and surface frost temperature. Because the vapor pressure of nitrogen frost is an extremely sensitive function of the frost temperature, changes in surface pressure inferred from occultations will translate to very tight constraints on the changing temperature of Pluto's nitrogen frost. Here we discuss the trend in Pluto's surface temperature in 1988, 2002, and 2006 in the context of Pluto's changing subsolar latitude and heliocentric distance.

Just as the martian atmosphere is supported by the vapor pressure of a surface constituent (carbon dioxide frost), Pluto's atmosphere is supported by the vapor pressure of nitrogen frost. Other volatiles that have been detected in the solid phase on Pluto's surface include CO and CH_4 . N_2 frost is by far the most volatile of these ices, and its latent heat of sublimation/condensation is thought to govern Pluto's nitrogen-covered surfaces to a globally constant temperature of ~ 40 K, regardless of the local diurnally-averaged solar flux (Spencer et al. 1997). The fact that Pluto's column abundance (or equivalently, its surface pressure) doubled between 1988 and 2002 implies that the global N_2 frost temperature increased by about 1.5 K over that period. This temperature increase occurred as the solar flux at Pluto decreased by 6% from 1988 to 2002 and by 9% from 1988 to 2006.

Hansen & Paige (1996) implemented a model to predict Pluto's surface temperature and pressure throughout a Pluto

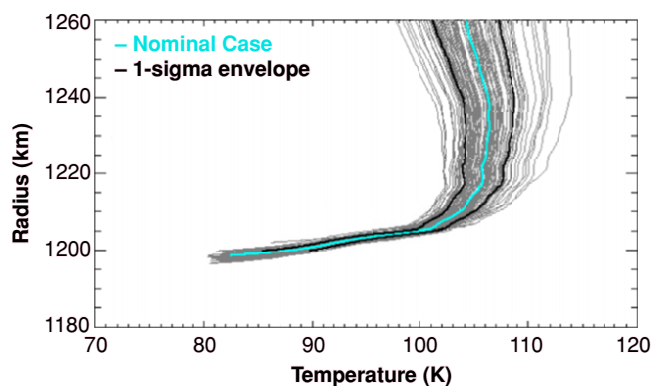


Figure 5. Error bars for the AAT ingress $T(z)$ profile, generated from 1000 Monte Carlo simulations. Appropriate noise was generated and added to the light curve in 1000 separate inversions, including noise propagated from the three-parameter upper boundary fits.

season. Free parameters included global values for the frost albedo, the substrate albedo, the column of available N_2 frost, the emissivity of N_2 frost and the thermal inertia of the surface. They considered solar heat input, thermal emission, conduction with subsurface layers, and the latent heats of the nitrogen α/β crystalline transition and the sublimation and condensation gas/frost transitions. They point out that small changes in certain parameters result in huge variations in the near-term surface pressure and temperature variations. There are, however, some common themes in all of the Hansen & Paige (1996) model predictions. The most striking of these is that Pluto's seasonal pressure peak will lag its perihelion (in 1989) by tens of years. A second result is that the pressure peak is usually (but not always) predicted to be tens of years in duration.

Figure 6 compares the change in pressure between the occultation observations in 1988, 2002, and 2006 to the predictions of four model runs from Hansen & Paige (1996). The best-fit prediction is Hansen & Paige (1996) run #38, with increases on pressure from 1988 to 2002 and 2006 that are just below the observed increases of around 2.1. This is a low thermal inertia, high frost emissivity scenario. It is interesting to note that run #34 is almost identical to run #38 except that the emissivity is lower (0.6 instead of 0.8) and the column of N_2 is half (50 kg m^{-2} instead of 100). The low emissivity translates to a much larger increase in Pluto's post-perihelion frost temperature (because the main cooling mechanism, thermal radiation, is inhibited) and much higher pressure increases than we observe from the occultations. It appears that the Hansen & Paige (1996) models could easily match the three occultation pressures observed to date by simply tweaking the frost emissivity to values slightly less than 0.8. Furthermore, both runs #34 and #38 predict only slightly diminishing pressures through 2015, the date of the *New Horizons* flyby.

4.2. The Non-Isotropic Temperature Profile of Pluto's Upper Atmosphere

From the AAT light curve we fit a temperature slope in Pluto's upper atmosphere (above a radius of 1275 km) of $-0.086 \pm 0.033 \text{ K km}^{-1}$, compared to -0.17 ± 0.05 found by Elliot et al. (2007). These are the first inferences of a statistically non-isothermal temperature gradient in Pluto's upper atmosphere at the 3σ level. This cooling-with-altitude trend may have been present in earlier occultations, but the S/N of earlier light curves was not high enough to infer a significant non-isothermal gradient.

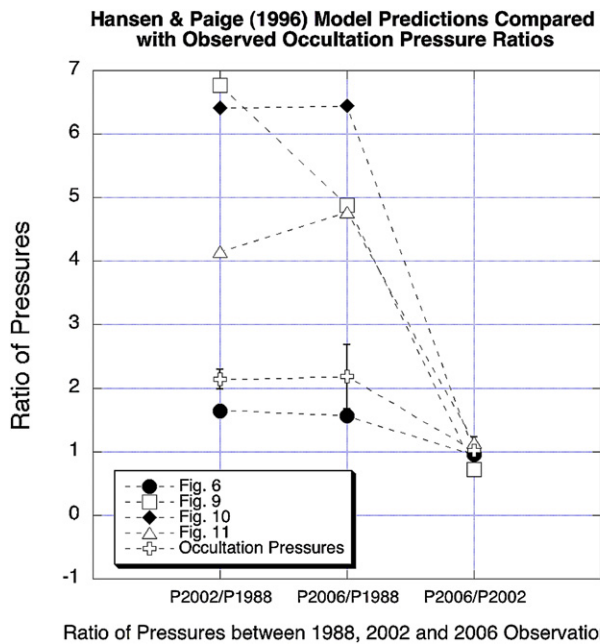


Figure 6. A comparison of Hansen & Paige (1996) model predictions to observed changes in pressure. The key refers to “Figures 6–11,” which are figure numbers in Hansen & Paige (1996) of various frost models. We plot ratios of pressures between 1988, 2002, and 2006 to avoid the issue of comparing surface pressures in the Hansen & Paige (1996) models to pressures at a reference altitude as observed in actual occultations. It is striking that several of the Hansen and Paige models are qualitatively eliminated on the basis of these three occultation measurements. While nearly all of the Hansen and Paige models predict little change between 2002 and 2006 (as observed), many models predict an increase in pressure between 1988 and 2002 or 2006 that exceeds the observed increase in pressure.

The finding of a negative temperature gradient is a significant milestone: it is circumstantial evidence for a cooling agent in Pluto’s upper atmosphere. The presence of a slight cooling trend with increasing altitude is consistent with the presence of CO, as pointed out by Strobel et al. (1996) and Elliot et al. (2007). CO has been detected as a surface frost in Pluto’s infrared spectrum, and CO is only 3–5 times less volatile than N₂ ice at the same temperature. CO has not yet been detected in the gas phase (Young et al. 2001), although Bockelée-Morvan et al. 2001 report a possible radio detection of the 2–1 transition. Gas-phase methane has been detected around the 3% level in Pluto’s atmosphere (Young et al. 1997).

Strobel et al. (1996) implemented a radiative-convective model to estimate the vertical temperature structure of Pluto’s atmosphere. They considered heating and cooling in the CH₄ bands at 2.3, 3.3, and 7.6 μm, cooling by emission via CO’s rotational lines, and conduction of heat between layers in the atmosphere. In one example (0.05% CO, 3% CH₄), they found a thermal gradient of -0.05 K km^{-1} in Pluto’s upper atmosphere.

The detection of gas-phase CO would have consequences for our understanding of Pluto’s upper atmosphere. CO acts as a universal coolant, continually converting kinetic energy to radiation. Even trace amounts of gas-phase CO would cool Pluto’s upper atmosphere, compress scale heights, and reduce the rate at which Pluto’s atmosphere escapes to space.

4.3. Temperature Perturbations in Pluto’s Lower Atmosphere

We performed an inversion (Figure 4) under the clear atmosphere/no far-limb assumptions. In both of the AAT light

curves, there are spikes corresponding to local temperature fluctuations at radii of around 1230 km down to ~ 1200 km, which is as low as we can probe. These spikes are suggestive of gravity waves. The egress temperature gradient has three cycles (four peaks) between 1206 and 1227 km, consistent with a vertical wavelength of ~ 7 km in this range. We see no significant perturbations above 1230 km. In the ingress temperature gradient profile, there are four cycles between 1204 and 1215 km, with a vertical wavelength of approximately 2.7 km. Above 1215 km, we see a peak at 1221 km (6 km wavelength) and another at 1232 km (11 km).

If the perturbations in temperature are manifestations of gravity waves, then it should not be surprising that the vertical separation between temperature gradient minima seems to increase with altitude. In general, gravity waves with shorter wavelengths are damped more quickly than those with longer wavelengths. If the main damping mechanism is molecular diffusion, then damping is more effective in a less dense atmosphere. In this scenario, we would expect longer wavelengths to predominate at higher altitudes where damping of shorter wavelengths takes place more efficiently.

There are large, broad spikes in both the ingress and egress light curves (at a shadow radii of 710 km before the midevent and 790 km after midevent, respectively). These features correspond to large excursions in the temperature gradients. Above ~ 1207 km (Pluto radius), both the ingress and egress temperature gradient profiles are close to (but slightly greater than) the dry adiabat on Pluto, which is about -0.6 K km^{-1} . Below ~ 1207 km, there are excursions in the temperature gradients up to 8 K km^{-1} , much larger than the 0.5 to 0.7 K km^{-1} excursions that are seen in the perturbations above 1207 km.

4.4. Evidence for Global Circulation on Pluto

The temperature in the upper atmosphere for both ingress and egress is nearly the same in 2006 as it was in 2002 and 1988, highlighting the importance of 7.7 μm cooling by methane, which is extremely sensitive to temperature (Strobel et al. 1996). If atmospheric cooling is dominated by methane, then the 9% decrease incident solar flux between 1988 and 2006 will produce a decrease in the atmospheric mean temperature of less than 1 K. The nearly constant temperature of roughly 100 K in many atmospheres containing CH₄ is sometimes called the “methane thermostat” (e.g., Yelle & Lunine 1989).

However, the AAT immersion latitude (30.0 S) receives a diurnally-averaged incident insolation of 550 mW m^{-2} , while the emersion latitude (53.2 N), situated on the edge of uninterrupted night, receives only 0.37 mW m^{-2} . Without efficient transport of energy within Pluto’s atmosphere, the emersion temperatures would be tens of degrees K colder than those at immersion. For Pluto, predominantly an optically thin atmosphere at solar wavelengths, it is the time in sunlight that is important as opposed to the incident flux through a unit area which is perpendicular to the surface normal (Strobel et al. 1996). The ratio of diurnally-averaged times in sunlight between ingress and egress latitudes is still 7:1, and the upper atmosphere’s expected temperature at the egress latitude is 92 K. The observed temperature (egress) was $106.4 \pm 4.6 \text{ K}$, significantly higher than 92 K and nominally higher than the ingress temperature of $100 \pm 4.2 \text{ K}$. The implication is that radiative timescales in Pluto’s upper atmosphere are long compared to dynamical timescales.

Strobel et al. (1996) have estimated heating and cooling rates in Pluto’s atmosphere due to conduction, CH₄ heating

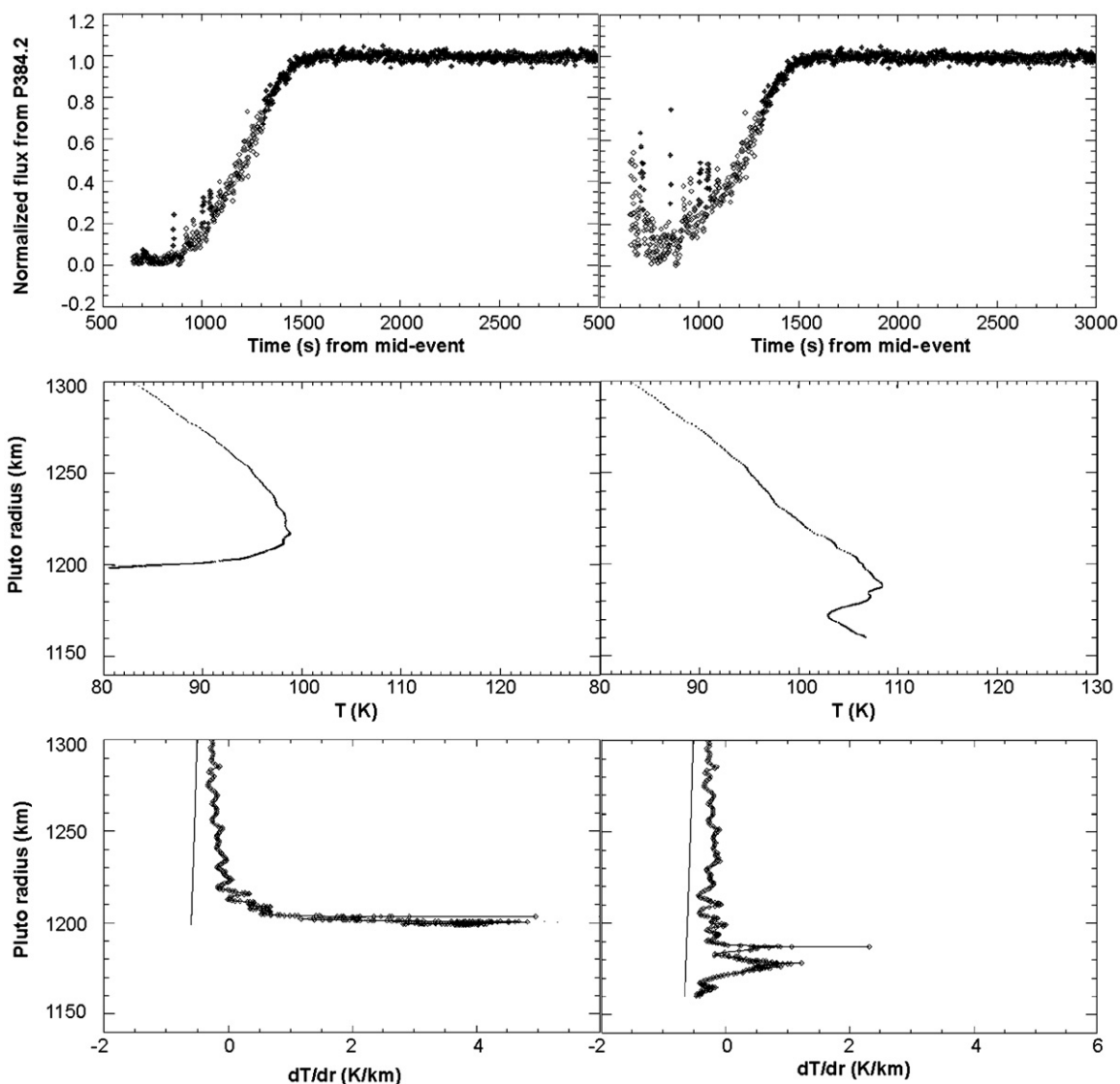


Figure 7. A “what-if” experiment to look at the temperature profile given an assumed haze profile. The left-side panels show (from top to bottom) the observed light curves, the temperature profiles as determined by the inversion method, and the temperature gradient profiles. The right column is identical to the left except that the haze parameters listed in Table 3 have been extrapolated to the lowest chords probed by the occultation. In the top row, the clear atmosphere light curve that remains after the assumed haze opacity is divided out (right panel) shows that the lower light curve would be brighter if the assumed haze opacity were not present. In the middle panels we see that the presence of haze (right) could explain the shape of the lower light curve just as well as a temperature inversion in the no-haze scenario (left), but the assumed-haze $T(z)$ profile reaches a radius of ~ 1150 km with temperatures over 100 K, a likely conflict with current estimates of Pluto’s solid radius. Finally, the main effect of an assumed haze distribution on the temperature gradients is to reduce the large dT/dz excursion associated with the temperature inversion. The nearly-vertical lines in the two lower panels are Pluto’s expected dry adiabat.

at 2.3 and 3.3 μm , CH_4 cooling at 7.7 μm , and CO cooling at 2.3 μm .

The 7.7 μm cooling term has the shortest timescale and is the primary avenue for cooling Pluto’s upper atmosphere. We calculate a time constant of $\tau_{7.7} = 0.5$ yr, assuming 3% CH_4 . This long time constant is dramatically different between Pluto and Mars. On Mars, the cooling time constant is on the order of hours, as evidenced by the dramatic amplitude of the martian diurnal temperature variation. On Pluto, with CH_4 as its primary cooling constituent, the cooling time constant is apparently much longer than the unknown dynamical timescales. We do not know the wind speeds between Pluto’s poles and equator, but if they are in the neighborhood of 10 m s^{-1} , they will produce dynamical timescales that are on the order of days, about two orders of magnitude faster than the radiative cooling timescale. In light of these relative rates, it is not surprising that the “methane thermostat” seems to be in effect over the

considerable range in latitudes that have been sampled by all previous occultations, even though some latitudes received very little insolation (Table 4).

4.5. Temperature Inversion Versus Haze Opacity

The 1988 occultation light curve showed a pronounced change in slope in both ingress and egress at the 1215 km level, prompting a vigorous discussion in the community as to the cause of that change. Could there be a haze layer below 1215 km (in 1988), or is there a thermal inversion in a clear atmosphere that attenuates the starlight by differential refraction? In this section we explore the temperature profile that would result if the exponential distribution of Pluto’s haze were extrapolated to the surface from the six-parameter fit to the upper atmosphere (Table 3).

Unlike our forward model, our inversion method assumes a clear atmosphere. We are not aware of an inversion code that

Table 4
Estimated Timescales in Pluto's Atmosphere at 1 μ bar

Dynamical timescale	$\tau_{\text{dyn}} = v/h$	~ 1.4 days	For $v = 10 \text{ m s}^{-1}$ and $h = 1850 \text{ km}$
Conduction timescale	$\tau_{\text{cond}} = \frac{\kappa}{rc_p d^2}$	~ 34 yr	For $d = H$ and negligible eddy diffusion
CH ₄ Cooling timescale at 7.7 μm	$\tau_{7.7} = \frac{1}{rc_p} \frac{dL_{7.7}}{dT}$	~ 0.5 yr	For 3% CH ₄ (Strobel et al. 1996)
CO Cooling timescale	τ_{CO}	~ 47 yr	For 0.046% CO (Strobel et al. 1996)

Notes.

- τ = timescale.
 v = characteristic horizontal wind speed.
 h = characteristic horizontal distance for winds to travel on Pluto.
 H = scale height ($\sim 55\text{--}60 \text{ km}$).
 κ = thermal conductivity (e.g., $\text{erg cm}^{-1} \text{ s}^{-1} \text{ K}^{-1}$).
 ρ = density.
 c_p = specific heat at constant pressure (e.g., $\text{erg K}^{-1} \text{ g}^{-1}$).
 d = characteristic vertical distance for conductivity.
 L = radiative cooling rate (e.g., $\text{erg cm}^{-1} \text{ s}^{-1}$).
 T = temperature.

incorporates haze opacity. In fact, to estimate the effect that haze opacity would have on Pluto's dT/dz profile, we pre-process the occultation light curves in a novel way; we assume a haze profile, then we normalize the observed light curve by $e^{\tau(s)}$, where $\tau(s)$ is the optical depth due to the assumed haze distribution along the instantaneous chord traversed by the light from the star. The effect of this normalization is to increase the flux of the lower light curve, since we are essentially removing the assumed attenuation due to haze, and that attenuation is greatest at the lowest altitudes.

Figure 7 shows the original AAT ingress light curve and that AAT light curve after it has been normalized by the assumed haze optical depth factor. When we invert the “de-hazed” AAT profile, we recover a temperature profile that is dramatically different from the clear atmosphere inversion. In the clear atmosphere case, a large temperature inversion at $\sim 1210 \text{ km}$ is required to explain the difference between the six-parameter fit to the upper atmosphere and the lower parts of the light curve. If a haze layer is extrapolated down to the surface (or as deep as the occultation probes), then no temperature inversion is required; the temperature just keeps getting warmer as we descend past 1210 km.

The presence of a large temperature inversion affects the mapping between points in the shadow and altitudes on Pluto. Without the temperature inversion, the bending angle at Pluto altitudes below 1210 km is less, which means that light curve points in the shadow map to lower altitudes on Pluto than they would in the clear atmosphere/thermal inversion case. With the assumed haze profile, we find that the temperature profile extends to altitudes below $\sim 1150 \text{ km}$, compared to 1198 km for the clear atmosphere case, and that the assumed-haze temperature profile is over 100 K at 1150 km.

The extrapolated-haze temperature profile is problematic for two reasons. First, preliminary results from mutual event photometry indicate that Pluto's solid radius is 1153 km (Tholen & Buie 1997). If we find that the occultation probes altitudes below the mutual event solid radius, then it is likely that the mapping between the shadow radius and Pluto's radius is incorrect, which in turn implies that the derived temperature profile is wrong. Second, even if the extrapolated-haze temperature profile did indeed probe down to altitudes that lie just above Pluto's solid surface, the low-altitude temperatures of over 100 K are much higher than the known surface temperature of $\sim 40 \text{ K}$. For these two reasons we believe that a thermal inversion

is at least partially responsible for the discrepancy between the nearly isothermal fit to the upper atmosphere and the observed flux transmitted through the lower atmosphere.

5. CONCLUSIONS

In summary, the high-quality AAT light curve lets us make progress on four fronts with respect to ongoing Pluto investigations. First, we can constrain surface/atmosphere models which predict a shrinking (or expanding) atmosphere by 2006. In the context of the Hansen & Paige (1996) simulations, we rule out their scenarios in which the frost emissivity is low. Second, we constrain the horizontal dynamics and energetics in Pluto's atmosphere by showing similar temperature profiles in summer and winter hemispheres. Although the uniformity of the upper atmosphere temperature of $\sim 104 \text{ K}$ might have been expected from the heating and cooling rates presented in Strobel et al. (1996) relative to speculative estimates for horizontal transport timescales, it is interesting that the observed ingress versus egress temperatures confirm this expectation. Third, we quantify temperature gradients and temperature fluctuations in Pluto's lower atmosphere: these results will eventually constrain vertical dynamics in Pluto's atmosphere. Finally, we constrain the amount of haze in Pluto's lower atmosphere and conclude that there must be a thermal inversion in Pluto's lower atmosphere.

The authors wish to give thanks for the considerable help they received from Martin George of the Launceston Planetarium, Peter Jaquiere and Ross Dicky of RASNZ, Alan Thomas and the staff of the NZ National Institute of Water and Atmospheric Research, Brian Carter and John Field of Carter Observatory, Beryl Wyatt of Wanaka, NZ, and the Dunedin Astronomical Society. The authors wish to acknowledge Norbert Zacharias, Marion Zacharias, and Trudy Tilleman of USNO for supporting astrometry. Portions of this work were supported by NASA Planetary Astronomy NNG05GF05G and NSF Major Research Instrumentation grant AST0321338.

Facilities: AAT.

APPENDIX

INVERSION METHOD

Elliot et al. (2003, EPQ03 henceforth) extended the inversion method (e.g., French et al. 1978) to small planets, giving

equations for radius r , bending angle θ , refractivity ν , number density n , pressure p , and temperature T given the observed flux ψ and position in the occultation shadow y under the following assumptions: (i) the scale height is small compared to the radius, (ii) the refractivity is a function of only altitude, (iii) the atmosphere has uniform composition, (iv) the atmosphere is in hydrostatic equilibrium, (v) extinction is negligible when compared to the decrease in intensity due to refraction, (vi) the occulted star is a point source, (vii) diffraction effects are negligible, (viii) there is no ray-crossing, and (ix) bending angles are small.

For a set of shells with midpoints i , EPQ03 give equations for r , p , n , ν , and T at the lower boundary of the shells, $i + 1/2$. EPQ03 do not give an explicit equation for calculating temperature derivatives. While derivatives at the shell midpoints can be derived from the temperatures and radii at the shell boundaries, this has two drawbacks. First, an explicit equation for T can yield insight into the area of the atmosphere influencing the observations (French et al. 1978). Second, atmospheric variables such as conductive heating and the Brunt–Väisälä frequency depend on both temperature and its derivative. Interpolating the temperature and radius to the shell midpoint can lead to a loss of precision. We, therefore, derived equations for the derivatives of refractivity, number density, and temperature with respect to radius evaluated at shell boundaries.

We begin the equation for refractivity from EPQ03, their Equation (16):

$$\nu(r) = \frac{1}{\pi} \int_r^\infty \cosh^{-1} \left(\frac{r'}{r} \right) \frac{d\theta(r')}{dr'} dr'. \quad (\text{A1})$$

We can take the derivative of $\nu(r)$ with respect to r by taking the derivative of r within the integral, leaving r' constant (because $\cosh^{-1}(1) = 0$):

$$\frac{d\nu(r)}{dr} = \nu'(r) = -\frac{1}{\pi r} \int_r^\infty \frac{r'/r}{\sqrt{\left(\frac{r'}{r}\right)^2 - 1}} \frac{d\theta(r')}{dr'} dr'. \quad (\text{A2})$$

Following EPQ03, we write this as the sum of boundary integral, $B_{\nu'}$ for radii greater than a boundary radius, r_b , and a summation $I_{\nu'}$ over bins with radii less than r_b :

$$\nu'_{i+1/2} = \nu'(r_b, r_{i+1/2}) = B_{\nu'}(r_b, r_{i+1/2}) + S_{\nu'}(r_b, r_{i+1/2}) \quad (\text{A3})$$

where the boundary integral is the full integral over a smaller range

$$B_{\nu'}(r_b, r_{i+1/2}) = \frac{1}{\pi r} \int_0^{\theta(r_b)} \frac{r'/r}{\sqrt{\left(\frac{r'}{r}\right)^2 - 1}} d\theta \quad (\text{A4})$$

and the summation term is derived by “pre-integrating” (French et al. 1978). This assumes that $d\theta/dr$ changes slowly over each shell, and can be pulled out of the integral in Equation (A2), when the limits of the integral are the shell boundaries

$$S_{\nu'}(r_b, r_{i+1/2}) = \frac{1}{\pi} \sum_{j=j_b}^i \frac{[\sqrt{z^2 - 1}]_{z_{j-}}^{z_{j+}}}{z_{j+} - z_{j-}} \Delta\theta_j. \quad (\text{A5})$$

As in EPQ03, $z_{j+} = r_{j+1/2}/r_{i+1/2}$ and $z_{j-} = r_{j-1/2}/r_{i+1/2}$. Equation (A2) for ν' is analogous to Equations (16) and (27) for ν and p in EPQ03, Equation (A3) is analogous to EPQ03 (54) and (56), Equation (A4) is analogous to EPQ03 Equations (35) and (36), and Equation (A5) is analogous to EPQ03 Equations (37) and (38).

Given $\nu'(r) = d\nu(r)/dr$ from the equations given here, and ν , p , H , and T from EPQ03, and assuming (as in EPQ03) that the composition is constant with altitude, we can also derive the temperature gradient:

$$T'(r) = \frac{dT(r)}{dr} = T \left(\frac{1}{\nu} \frac{d\nu(r)}{dr} - \frac{1}{H} \right). \quad (\text{A6})$$

REFERENCES

- Baum, W. A., & Code, A. D. 1953, *AJ*, **58**, 108
 Bockelée-Morvan, D., et al. 2001, *A&A*, **377**, 343
 Brosch, N., & Mendelson, H. 1985, *IAUC*, 4097
 Brown, G. N., & Ziegler, W. T. 1980, *Adv. Cryog. Eng.*, **25**, 662
 Cox, A. 2000, *Allen's Astrophysical Quantities* (4th ed; Berlin: Springer)
 Elliot, J. L., Person, M. J., & Qu, S. 2003, *AJ*, **126**, 1041
 Elliot, J. L., & Young, L. A. 1992, *AJ*, **103**, 991
 Elliot, J. L., et al. 1989, *Icarus*, **77**, 148
 Elliot, J. L., et al. 2003, *Nature*, **424**, 165
 Elliot, J. L., et al. 2007, *AJ*, **134**, 1
 Eshelman, V. R. 1989, *Icarus*, **80**, 439
 French, R. G., Elliot, J. L., & Gierasch, P. J. 1978, *Icarus*, **33**, 186
 Grundy, W. M. 1995, *Methane and Nitrogen Ices on Pluto and Triton: a Combined Laboratory and Telescope Investigation*, PhD thesis, Univ. of Arizona
 Hansen, C. J., & Paige, D. A. 1996, *Icarus*, **120**, 247
 McDonald, S. W., & Elliot, J. L. 2000a, *AJ*, **119**, 1999
 McDonald, S. W., & Elliot, J. L. 2000b, *AJ*, **120**, 1599
 Pasachoff, J. M., et al. 2005, *AJ*, **129**, 1718
 Roques, F., et al. 1994, *A&A*, **288**, 985
 Sicardy, B., et al. 2003, *Nature*, **424**, 168
 Spencer, J. R., et al. 1997, *Pluto and Charon*, 435
 Strobel, D. F., et al. 1996, *Icarus*, **120**, 168
 Tholen, O. J., & Buie, M. W. 1997, *Icarus*, **125**, 245
 Tryka, K. A., et al. 1994, *Icarus*, **112**, 512
 Yelle, R. V., & Lunine, J. I. 1989, *Nature*, **339**, 228
 Young, L. A., et al. 1997, *Icarus*, **127**, 258
 Young, L. A., et al. 2001, *Icarus*, **153**, 148
 Young, L. A., et al. 2005, *Icarus*, **175**, 185